Int. J. Electrochem. Sci., 15 **(2020)** 2776 – 2791, doi: 10.20964/2020.03.42

International Journal of
ELECTROCHEMICAL
SCIENCE
www.electrochemsci.org

Co_3O_4@$MnMoO_4$ Nanorod Clusters as an Electrode Material for Superior Supercapacitors

Danfeng Cui[1,], Yanfang Li[1], Yuankai Li[1], Yanyun Fan[1], Hongmei Chen[1], Hongyan Xu[2] and Chenyang Xue[1]*

[1] Science and Technology on Electronic Test and Measurement Laboratory,North University of China, Taiyuan, Shanxi 030051, China
[2] School of Materials Science and Engineering, North University of China, Tai yuan, Shanxi 030051, China
[*]E-mail: cuidanfeng@nuc.edu.cn

Received: 29 October 2018 / *Accepted:* 20 December 2019 / *Published:* 10 February 2020

Co_3O_4@$MnMoO_4$ composites on nickel (Ni) foam were first synthesized by a two-step hydrothermal process and exhibited better electrochemical properties than pure Co_3O_4 nanorod clusters according to the electrochemical test. The specific capacities of the Co_3O_4 and Co_3O_4@$MnMoO_4$ electrodes are 436 $F \cdot g^{-1}$ and 663.75 $F \cdot g^{-1}$, respectively, at a current density of 2.5 mA cm^{-2}. After 3000 cycles, they Co_3O_4 and Co_3O_4@ $MnMoO_4$ electrodes retain 100% and 95.32% of the initial specific capacities, respectively, at a current density of 3 A g^{-1}. The great capacitive property of Co_3O_4@$MnMoO_4$ composites is attributed to their specific area, which leads to a higher electron/ion-transfer rate, more electroactive reaction sites and larger electrolyte infiltrate area than Co_3O_4 nanorod clusters.

Keywords: Co_3O_4@$MnMoO_4$, nanorod clusters, two-electrodes system, supercapacitors, high volumetric performance

1. INTRODUCTION

Supercapacitors have attracted increasing attention because of their excellent charge/discharge characteristics, wide operating temperature range, environmental friendliness, and safety[1-5]. They are applied to many portable systems and hybrid cars as the best power source. To date, because of their lower cost and toxicity and excellent morphology flexibility, the investigation of advanced electrode materials for Faraday capacitors has focused on transition metal oxides, hydroxides, or their combination[6], including NiO[7,8], CoO[9], $Ni(OH)_x$[6,10,11], $Co(OH)_x$[12-15], and MnO_2 [6,16-19].

Co_3O_4, with an extremely high theoretical capacitance, has excellent electroactivity as an electrode material of supercapacitors[20-22]. However, due to the limited redox reaction kinetics and unstable structure, these electrode materials generally have poor rate performance and cycling, which

limit their practical applications[6,23-27].

At present, molybdenum (Mo) composites include oxides[28-33], dihalides [34,35] and oxysalts [36-42]. Due to their high thermal/mechanical stability and other chemical/physical properties[43,49], they are considered as high efficient and promising electrochemical energy storage materials. Co_3O_4 and $MnMoO_4$ have attracted increasing attention due to their excellent electrochemical properties and environmental compatibility[44-50]. In addition to the individual contributions of their property features and internal structure as electrode materials, their electrochemical performance could be further enhanced the synergistic effect between Co_3O_4 and $MnMoO_4$[6].

Herein, Co_3O_4 nanorods and Co_3O_4@$MnMoO_4$ composites on Ni foam were first synthesized by hydrothermal method associated with annealing treatment. The Co_3O_4@$MnMoO_4$ composites could offer better electrochemical properties than the pure Co_3O_4 nanorods. Hybrid nanorod clusters shorten the electron transport distance and enhance the morphology flexibility of the Co_3O_4@$MnMoO_4$ electrode. At a current density of 2.5 mA cm^{-2}, the specific capacities of the Co_3O_4 and Co_3O_4@$MnMoO_4$ electrodes are 436 F g^{-1} and 663.75 F g^{-1}, respectively. After 3000 cycles, the Co_3O_4 and Co_3O_4@$MnMoO_4$ electrodes retained 100% and 95.32% of the initial specific capacities, respectively, at a current density of 3 A g^{-1}. The Co_3O_4@$MnMoO_4$//AC asymmetric electrodes achieved a high energy density of 12.03 Wh kg^{-1} at the power density of 0.3 kW kg^{-1} and has 80.59% capacitance retention at a current density of 5 A g^{-1}. The results show that Co_3O_4@$MnMoO_4$ composites have good application potential for super capacitors.

2. EXPERIMENTAL

2.1. Material preparation

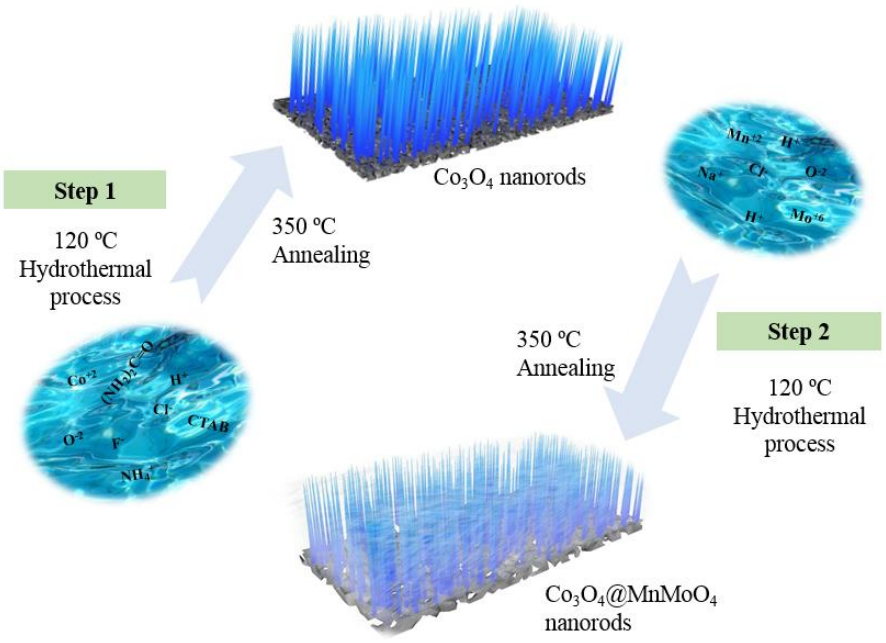

Figure 1. Schematic of Co_3O_4@$MnMoO_4$ composites preparation process

All reagents were of analytical grade (bought from the Sinopharm Chemical Reagent Co.Ltd. of China). The schematic fabrication process of Co_3O_4@$MnMoO_4$ composites on nickel foam is shown in Fig.1. First, the nickel foams were tailored to 1×1×0.1cm and pretreated with acetone, hydrochloric acid and ethyl alcohol, after ultrasonic washed with deionized (DI) water, dried at 80 °C for 6 h in an electrothermal blast oven. Finally, the Ni foams (1×1cm) used as substrate were weighed as m1.

2.1.1. Synthesis of Co_3O_4 nanorod clusters

The Co_3O_4 nanorod clusters were synthesized as follows: first, cobalt chloride hexahydrate ($CoCl_2 \cdot 6H_2O$) (5 mmol), ammonium fluoride (NH_4F) (10 mmol), carbamide ($CO(NH_2)_2$) (25 mmol) and hexadecyl trimethyl ammonium bromide (CTAB) (0.5 g) were dissolved by magnetic stirring for 1 h. Second, the mixture and a piece of precleaned Ni foam were kept at 120 °C for 10 h in a Teflon- lined stainless-steel autoclave. After a natural cooling process, the obtained Ni foam was calcined in air at 350 °C for 3 h with a heating rate of 1 °C min^{-1}.

2.1.2. Synthesis of Co_3O_4@$MnMoO_4$ nanorod clusters

The Co_3O_4@$MnMoO_4$ nanorod clusters were synthesized as follows: manganese (II) chloride tetrahydrate ($MnCl_2 \cdot 4H_2O$) (2.5 mmol) and sodium molybdate dihydrate ($Na_2MoO_4 \cdot 2H_2O$) (2 mmol) were mixed in DI water by magnetic stirring for 30 min. And then the mixture and the as-prepared Co_3O_4 nanorod clusters on the Ni foam were kept at 120°C for 10 h. After a natural cooling process, the obtained Ni foam was calcined under the same conditions as in the synthesis of the Co_3O_4 nanorod clusters.

2.1.3. Mass Calculation of Electrode Materials

The mass of the Co_3O_4 covering the nickel foam (1×1cm) is m2, and the mass of the Co_3O_4@ $MnMoO_4$ covering the nickel foam (1×1cm) is m3. The mass of Co_3O_4 and Co_3O_4@$MnMoO_4$ can be calculated according to the equations as followed and the calculation process was repeated several times to minimize errors:

$$m_{Co3O4}(wt\%) = m2 - m1 \quad (1)$$

$$m_{Co3O4@MnMoO4}(wt\%) = m3 - m1 \quad (2)$$

The mass of Co_3O_4 and Co_3O_4@$MnMoO_4$ covering the Ni foam was 2.5 mg·cm^{-2}.

2.2. Characterization of Co_3O_4 and Co_3O_4@$MnMoO_4$ nanorod Clusters

X-ray diffraction (XRD) analyses were performed using a Bruker D8 (Germany) with Cu Kα (λ=0.15406 nm) radiation in the 2θ range of 10-80° at 40 eV. The morphologies and microstructures of the Co_3O_4 and Co_3O_4@$MnMoO_4$ nanorod clusters were characterized using a Scanning Electron Microscopy (SEM, SU-5000, Japan) and High-Resolution Transmission Electron Microscopy (HRTEM,

FEI Tecnai G2 F30, USA). The Brunauer-Emmett-Teller (BET) analyses and N_2 adsorption desorption isotherm curves were obtained using a Quantachrome Instruments (QuadraSorb SI, USA).

2.3. Electrochemical measurements

The as-achieved Co_3O_4 and Co_3O_4@$MnMoO_4$ nanorod clusters on Ni foam were used as the working electrodes in an aqueous KOH electrolyte of 3 mol L^{-1} at room temperature for constant current charge/discharge, cyclic voltammetry (CV), and electrochemical impedance spectroscopy (EIS) via an electrochemical workstation (Instruments, RST5000, China).

In three-electrode system, saturated Ag/AgCl and platinum plate electrodes are served as the reference and counter electrodes, respectively. The galvanostatic charge-discharge data is used to calculate the specific capacitance according to the equation as followed [22,51]:

$$C = \frac{I \cdot t}{m \cdot \Delta V} \quad (3)$$

where t, I, m, ΔV and C are the discharging time (s), discharging current (A), mass of the active material (g), potential drop (V) during discharging, and mass specific capacitance ($F \cdot g^{-1}$), respectively [21].

The asymmetric electrodes of Co_3O_4@$MnMoO_4$//AC was measured by using a two-electrode system to investigate the application potential of Co_3O_4@$MnMoO_4$. The quality ratio of the Co_3O_4@ $MnMoO_4$ and activated carbon(AC) was calculated as follows[52,53]:

$$Q_+ = Q_- \text{ and } \frac{m_+}{m_-} = \frac{C_+ V_+}{C_- V_-} \quad (4)$$

where Q_+ and Q_- are the positive electrode charge and negative electrode charge, V is the potential change during discharge, and C is the specific capacitance. The total mass of the Co_3O_4@$MnMoO_4$// AC asymmetric electrodes is 5.5 mg. The energy and power densities were at different current densities. The energy (E) and power (P) densities which were derived from charge-discharge curves are calculated as followed[54]:

$$E = \frac{1}{2} C \cdot \Delta V^2 \quad (5)$$

$$P = \frac{E}{\Delta t} \quad (6)$$

where C, Δt and ΔV are the specific capacitance ($F \cdot g^{-1}$), the discharge time (s) and the potential window (V), respectively.

3. RESULTS AND DISCUSSION

3.1 Structural and morphological analysis

Fig.2 shows the XRD patterns of the Co_3O_4 and Co_3O_4@$MnMoO_4$ nanorod clusters. According to the JCPDS card (PDF#42-1467), the XRD peaks of Co_3O_4 at 2θ = 19.00, 31.27, 36.85, 38.54, 44.81,

55.66, 59.36 and 65.24 are for the (111), (220), (311), (222), (400), (422), (511) and (440) planes, respectively. This illustrates that the Co_3O_4 whose space group is cubic Fd3m (227) for the nanorod clusters has a special structure. The peaks of Co_3O_4@$MnMoO_4$ are in agreement with the JCPDS card (PDF#50-1287) at 2θ = 18.83, 22.70, 25.70, 27.71, 33.01 and 51.13, which respond to (-201), (021), (-220), (-311), (-222) and (-204) planes, respectively. This shows that the $MnMoO_4$ crystals have a monoclinic structure (space group:C2/m (12)).

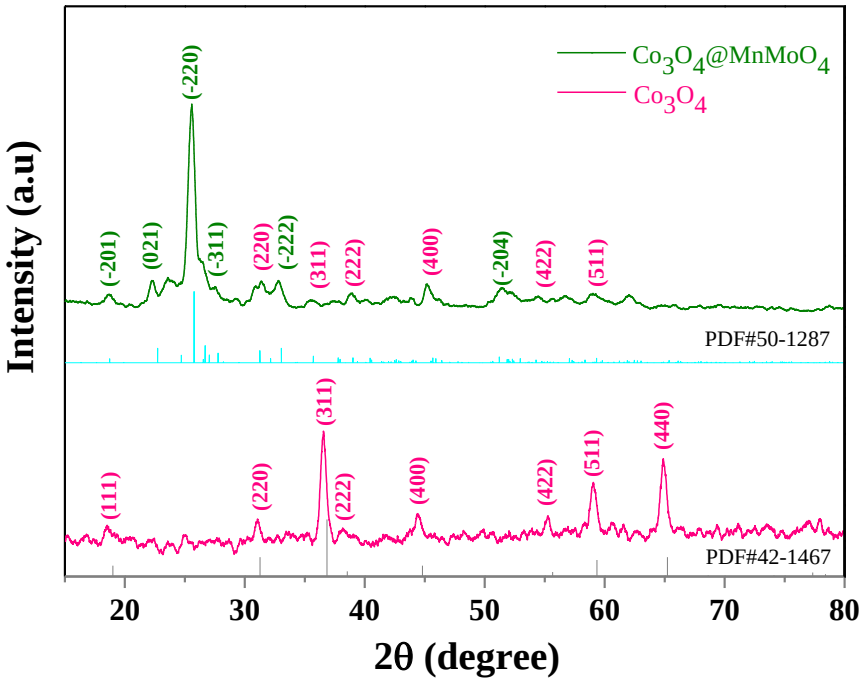

Figure 2. the XRD of Co_3O_4 and Co_3O_4@$MnMoO_4$

The purpose of the BET surface analysis is to investigate the pore size distribution and specific surface area of Co_3O_4 and Co_3O_4@$MnMoO_4$ nanorod clusters. The typical IV sorption behaviour with a hysteresis loop in the range of 0.2–1.0 P/P_0 according to Fig.3(a) and Fig.3(b). This special phenomenon indicates the existence of mesopores. The distributions corresponding to the Barrett- Joyner-Halenda (BJH) pore size are shown in Fig.3(c) and Fig.3(d). The BET specific area of Co_3O_4 and Co_3O_4@$MnMoO_4$ are 37.55 $m^2 \cdot g^{-1}$ and 44.13 $m^2 \cdot g^{-1}$, respectively. The BJH desorption pore volume of Co_3O_4 and Co_3O_4@$MnMoO_4$ are 0.181 $cm^3 \cdot g^{-1}$ and 0.147 $cm^3 \cdot g^{-1}$, respectively. According to the pore distributions, the pore sizes of Co_3O_4 and Co_3O_4@$MnMoO_4$ nanorod clusters are uniform within the range of 3–40 nm.

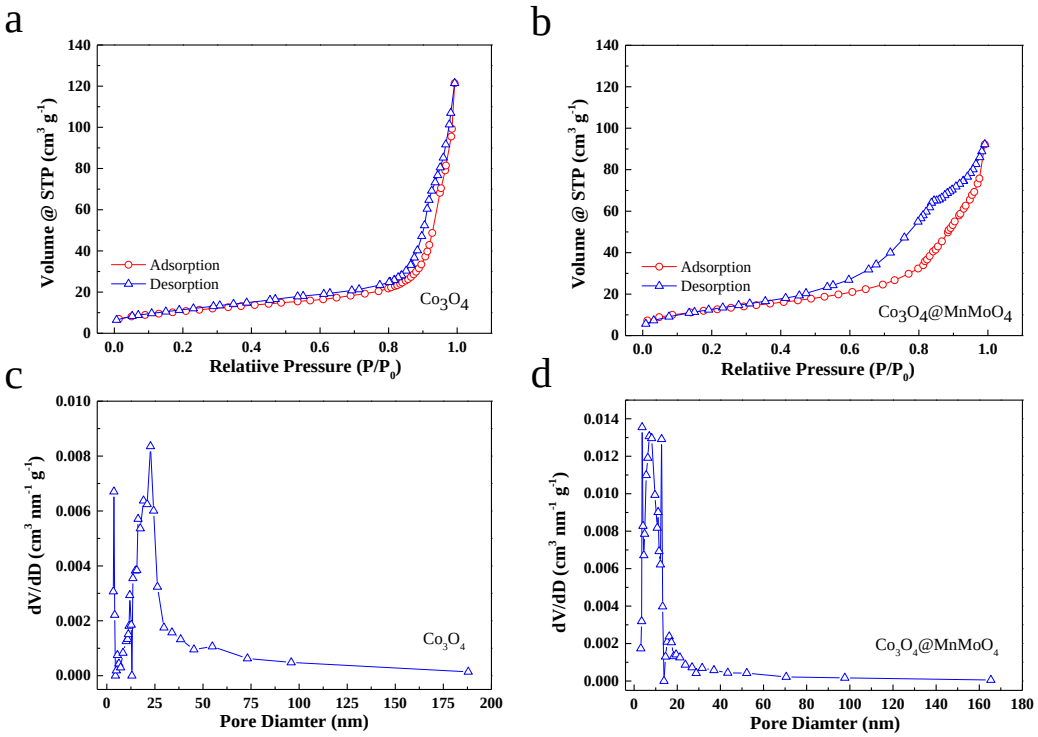

Figure 3. N_2 adsorption-desorption isotherms (a and b) and pore size distributions (c and d) of Co_3O_4 and Co_3O_4@$MnMoO_4$ nanorod clusters

The SEM images of Co_3O_4 nanorod clusters are shown in Fig.4(a-f) while the TEM images are shown in Fig. 4(g) and Fig. 4(h). According to the SEM and TEM images, the diameter of the Co_3O_4 nanorods is ~100 nm. Fig.4(i) and Fig.4(j) are the HRTEM micrograph and SAED pattern of Co_3O_4 nanorods. The results indicate that the inter-fringe distances of the nanorods are 0.286, 0.244, 0.20, 0.156 and 0.143 nm, which are compatible with the (220), (311), (400), (511) and (440) planes of the Co_3O_4 spinel structure, respectively. Fig.4(k) is the EDS mapping of Co_3O_4 nanorods which shows the uniform distribution of O and Co in Co_3O_4 nanorods.

The SEM and TEM images of Co_3O_4@$MnMoO_4$ nanorod clusters are shown in Fig.5 (a-f) and Fig.5(g), respectively. According to the SEM and TEM images, the Co_3O_4 nanorods were evenly covered with sheets of $MnMoO_4$, which formed nanorod clusters of Co_3O_4@$MnMoO_4$ composite. The SAED pattern and HRTEM micrograph of Co_3O_4@$MnMoO_4$ composite are shown in Fig.5(h) and Fig.5(i). The results showed that the sizes of the interstrip distances of $MnMoO_4$ are 0.169 and 0.471 nm, which are in good agreement with the $MnMoO_4$ monoclinic structure planes (530) and (-201), respectively. The EDS mapping of the Co_3O_4@ $MnMoO_4$ composite is shown in Fig. 5(j), which shows the uniform distribution of O, Co, Mn and Mo in the Co_3O_4@$MnMoO_4$ composite.

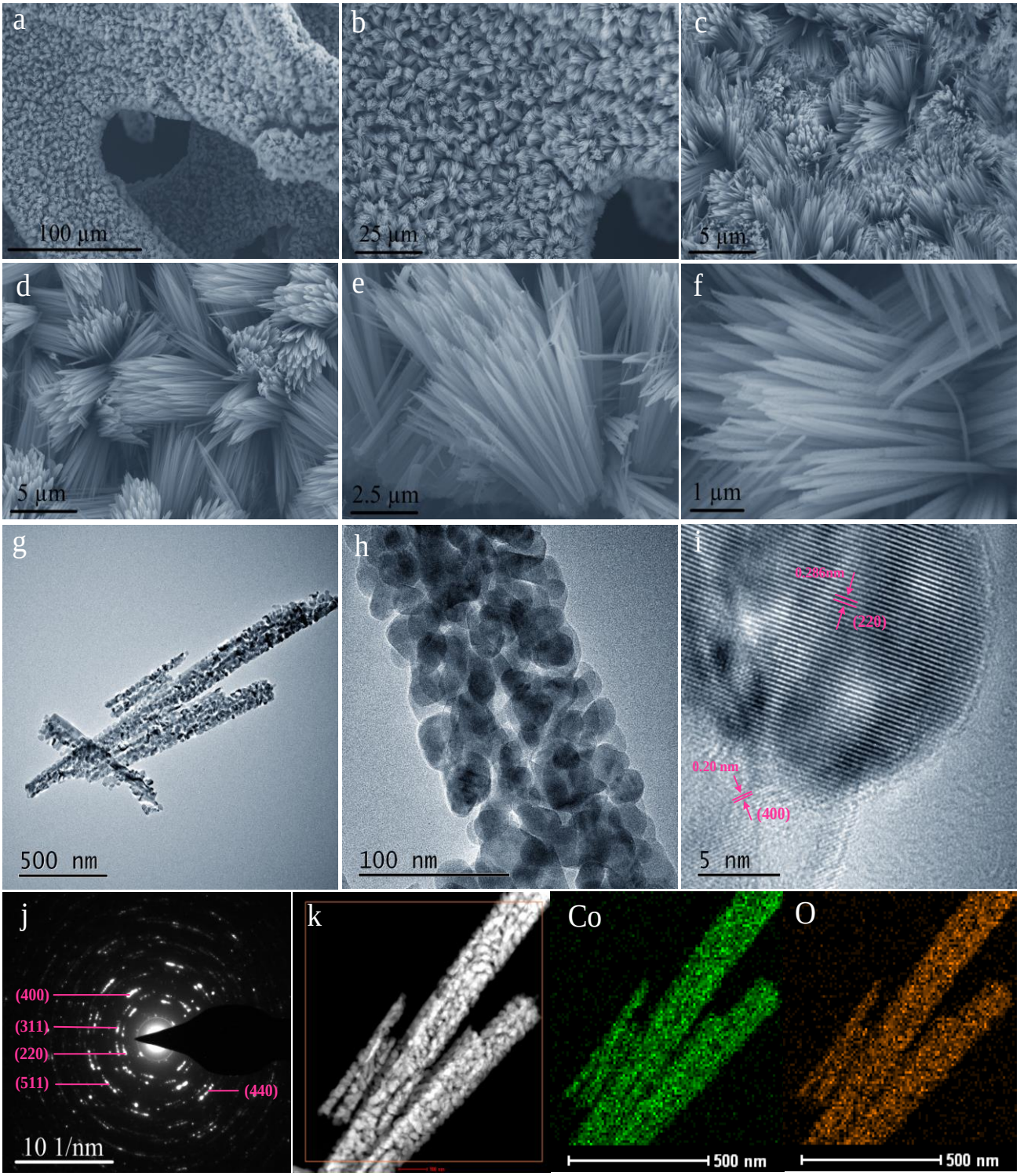

Figure 4. The SEM (a-f), TEM (g and h), HRTEM (i), SAED (j) and EDS mappings (k) of Co and O elements of Co_3O_4 nanorod clusters

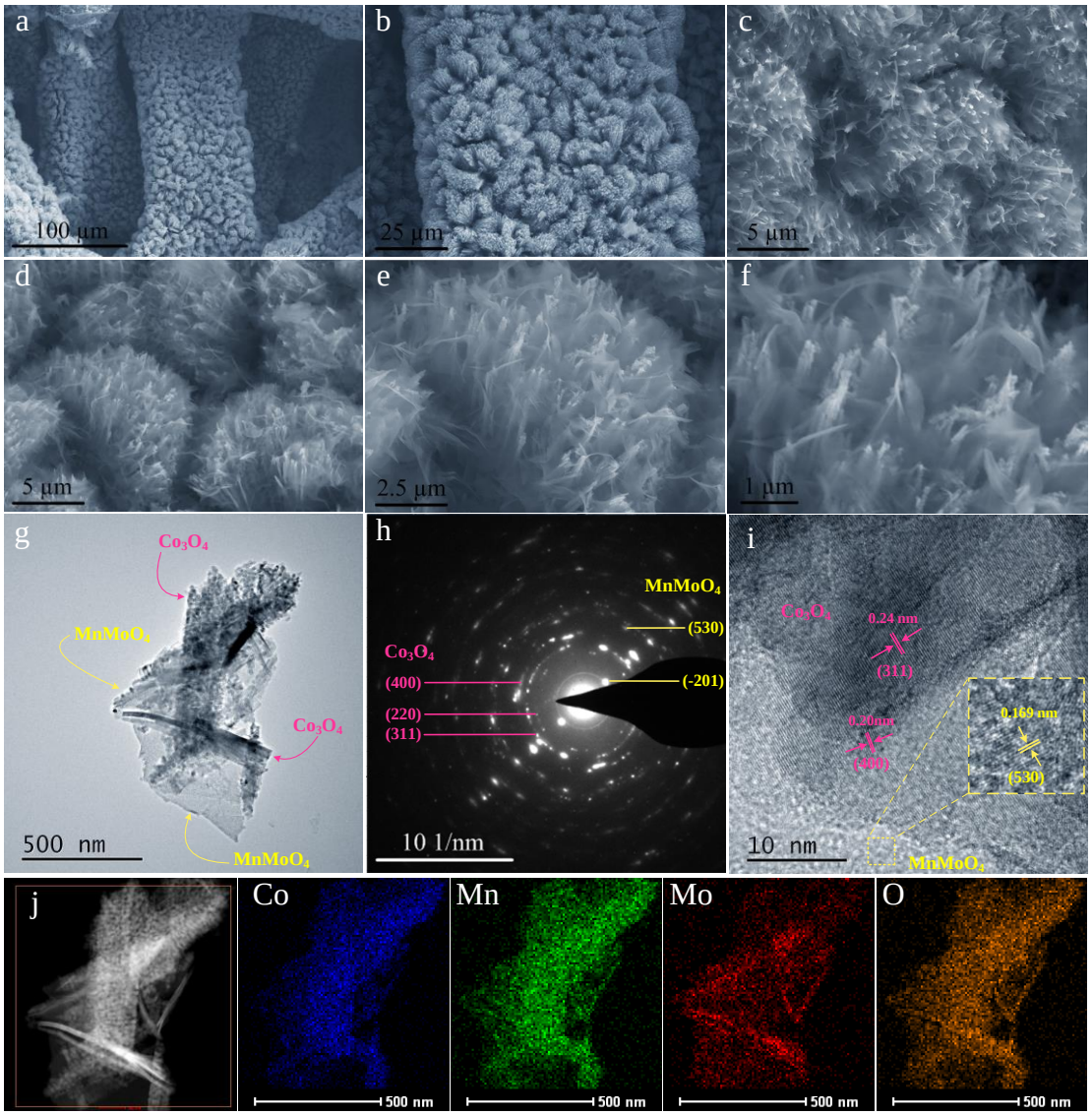

Figure 5. The SEM (a-f), TEM (g), SAED (h), HRTEM (i) and EDS mappings (j) O and Co of Co_3O_4@$MnMoO_4$ composites

3.2 Electrochemical measurements

By using aqueous 3 mol/L KOH in a three-electrode configuration, successful execution of the electrochemical tests with the Co_3O_4 and Co_3O_4@$MnMoO_4$ electrodes was achieved. Fig. 6 shows the cyclic voltammetry (CV) curves with scanning speeds of 5, 10, 30, 50, 80 and 100 mV s^{-1}. The Faradaic redox reactions dominate the main pseudocapacitive reaction process, resulting in visible redox peaks on every CV curve. The Ni foam signal is very small and its capacitance is negligible. Fig.7(a) shows the CV curves of the Co_3O_4 and Co_3O_4@$MnMoO_4$ electrodes with scanning speeds of 5 mVs^{-1}. Observably, the enclosed areas of the Co_3O_4@$MnMoO_4$ composites in the current-potential curve are larger than those of the Co_3O_4 nanorods, which means the Co_3O_4@$MnMoO_4$ have a larger area specific capacitance. Fig. 6(b) and (c) show that the peak potential shifted when the scan rate increased because of the electrode polarization.

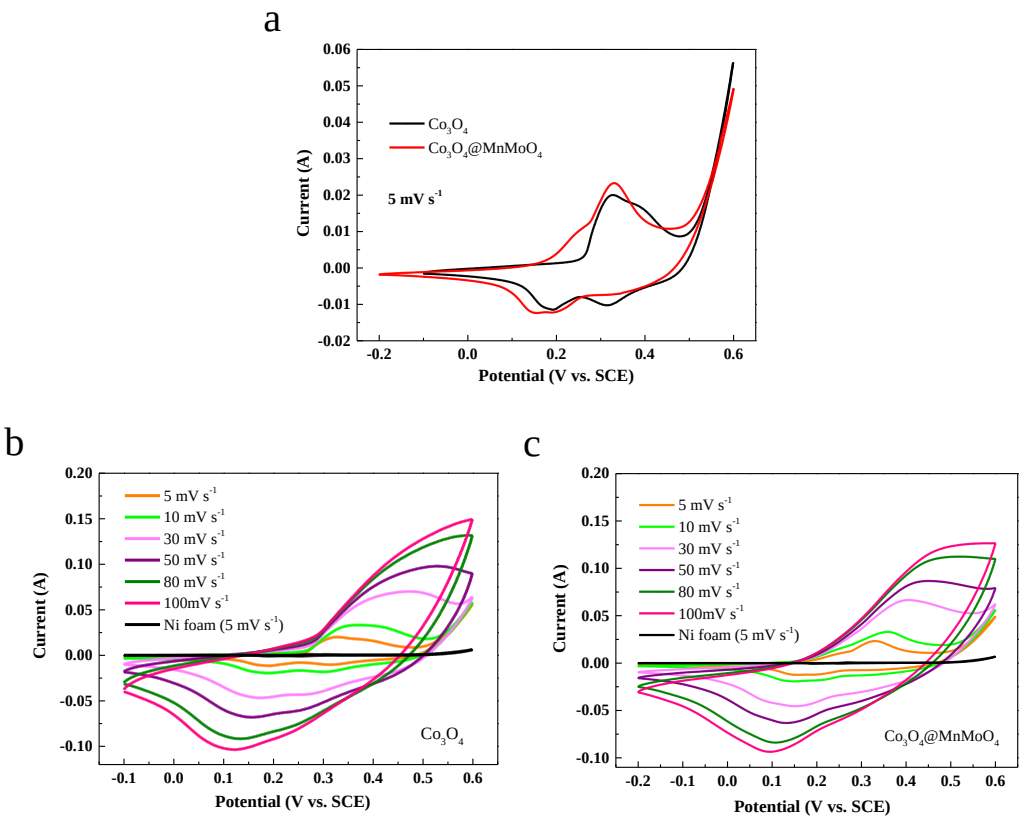

Figure 6. CV curves of Co_3O_4 nanorods (a, b) and Co_3O_4@$MnMoO_4$ composites (a, c) at various scan rates.

The galvanostatic charge-discharge curves of the Co_3O_4 and Co_3O_4@$MnMoO_4$ were obtained at different current densities of 1.0, 2.5, 5.0, 7.5, 10 and 15 mA cm^{-2}, as shown in Fig. 7(a) and (b). Fig. 7(c) shows the specific capacitances of the Co_3O_4 and Co_3O_4@ $MnMoO_4$ electrodes at different current densities. At different current densities of 1.0, 2.5, 5.0, 7.5, 10 and 15 mA cm^{-2}, the specific capacitances of the Co_3O_4@$MnMoO_4$ electrode were 664.4, 663.75, 557, 497.25, 456 and 399 F g^{-1}, respectively, higher than those of the Co_3O_4 electrode of 469.8, 436, 392.5, 362.25, 336 and 294 F g^{-1}. The capacitance of the Co_3O_4@$MnMoO_4$ electrode is better than that of Co_3O_4 because of the larger contact area between the electrolyte solution and the Co_3O_4@ $MnMoO_4$ composites.

The cyclic stabilities of the Co_3O_4 and Co_3O_4@$MnMoO_4$ electrodes were evaluated at a constant current density of 3 A g^{-1} in range of 0-0.4 V for 3000 cycles, as shown in Fig.7(d). The initial specific capacitances of the Co_3O_4 and Co_3O_4@$MnMoO_4$ electrodes are 362.25 and 497.25 F g^{-1}, respectively, at a current density of 3 A g^{-1}. After 3000 cycles, the specific capacitance of Co_3O_4@$MnMoO_4$ is 474 F g^{-1} with a capacity retention ratio of 95.32%, while that of Co_3O_4 is 362.25 F g^{-1} and retains 100% of the initial specific capacitance. The cycling performance of the Co_3O_4 and Co_3O_4@$MnMoO_4$ electrodes are all relatively stable.

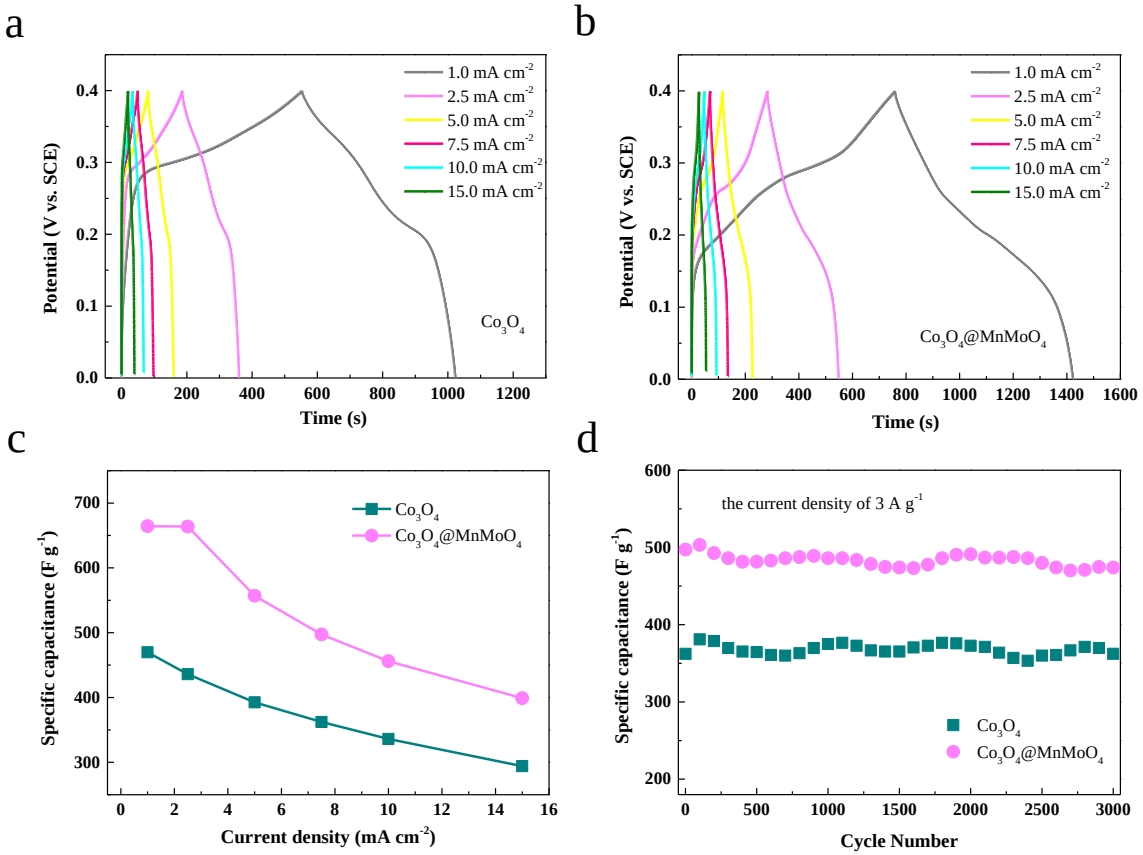

Figure 7. The galvanostatic charge-discharge curves (a, b), specific capacitances (c) and cycling performance (d) of Co_3O_4 and Co_3O_4@$MnMoO_4$ electrodes.

Electrode materials were analyzed using electrochemical impedance spectroscopy (EIS), including the redox reaction resistance, the equivalent series resistance and the electrochemical frequency of a system[51]. The Nyquist plots of the Co_3O_4 and Co_3O_4@$MnMoO_4$ electrodes in the frequency range from 10 kHz to 0.01 Hz with an ac perturbation amplitude of 5 mV are shown in Fig. 8. R_s, C_f, C_{dl}, Q, W, T and R_{ct} are the resistance of the solution in the equivalent circuit diagram, Faraday pseudocapacitance[51], double-layer capacitance, constant phase angle elements, Warburg impedance (Z_w), barrier diffusion impedance (Z_T) and Faraday interface charge transfer resistance. According to the data, the solution resistances of the Co_3O_4 and Co_3O_4@$MnMoO_4$ electrodes are 0.7752 and 0.6867 Ω, respectively, and those of the charge transfer resistances are 1.408 and 1.113 Ω, respectively. This indicates that the electrical conductivity of the Co_3O_4@$MnMoO_4$ electrode is better than that of the Co_3O_4 electrode, which determines its electrochemical properties.

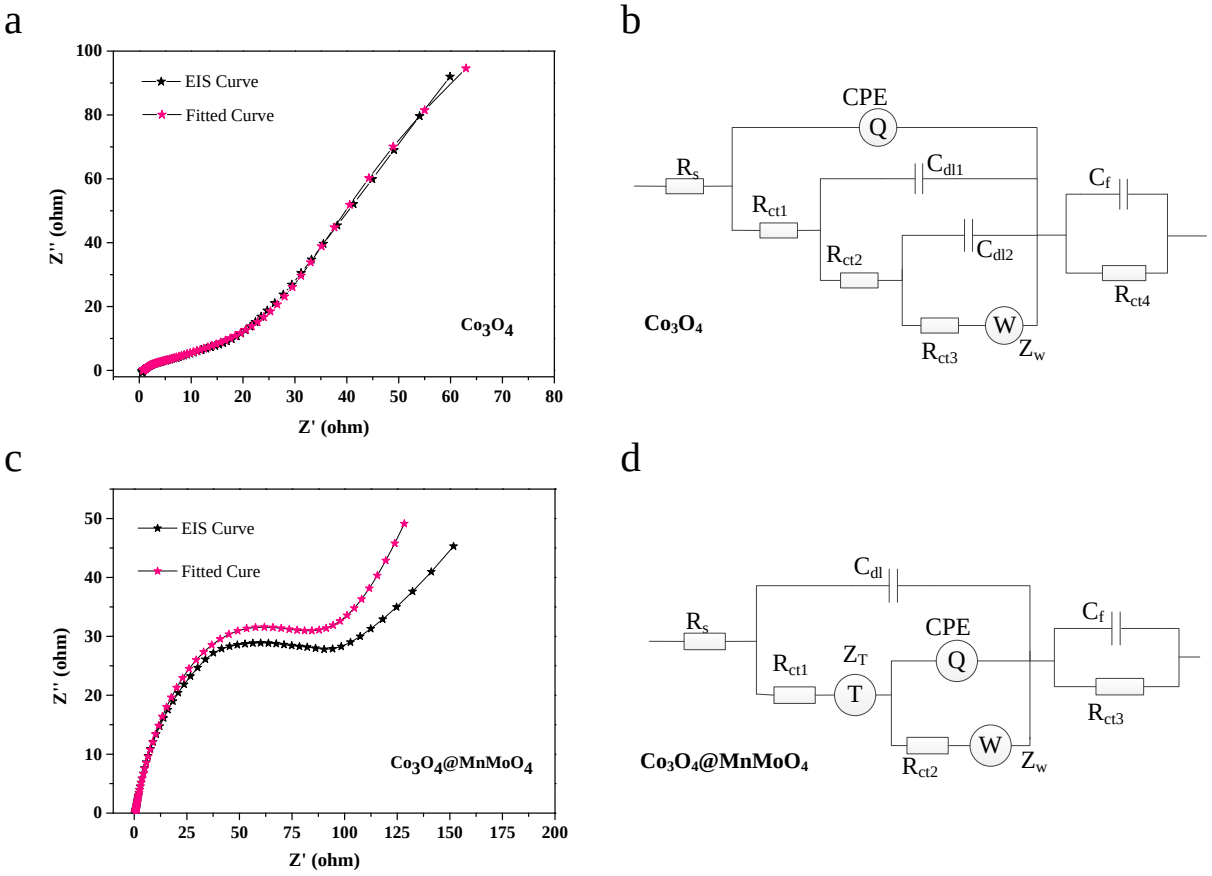

Figure 8. EIS plots (a, c) and equivalent circuit diagrams (b, d) of Co_3O_4 and Co_3O_4@$MnMoO_4$ electrodes

Using asymmetric electrodes to measure the capacitance performance of the double electrode system, the potential of Co_3O_4@$MnMoO_4$ as the positive electrode was further investigated. Fig. 9(a) and (b) show the CV and the charge-discharge curves of the AC electrode tested in a tripolar system at different potential windows of 0.4, -0.6, -0.8 and -1.0 V and at different current densities of 1, 2.5, 5, 10 and 20 mA cm^{-2}, respectively. Fig.9(c) shows the CV curves of the AC and Co_3O_4@$MnMoO_4$ electrodes in the potential window from -0.6 to 0.6. The CV curves of the Co_3O_4@$MnMoO_4$//AC asymmetric electrodes at different potentials of 0.6, 0.8, 1.0 and 1.2 V are shown in Fig. 9(d), which were tested at a scanning speed of 50 mV s^{-1} in a two-electrode system.

Fig. 10(a) and (b) are the CV and charge-discharge curves of the Co_3O_4@ $MnMoO_4$//AC asymmetric electrodes at different scan rates and current densities, respectively. Fig.10(c) shows the specific capacities and capacitance retention of the Co_3O_4@$MnMoO_4$//AC system at different current densities. At a current density of 0.5 A g^{-1}, the specific capacity of the Co_3O_4@ $MnMoO_4$//AC system is 60.17 F g^{-1}. The current density of this system is 5 A g^{-1} with a capacitance retention ratio of 80.59%. The energy densities of the Co_3O_4@$MnMoO_4$//AC are shown in Fig.10(d) at different power densities. At the power density of 0.3 kW kg^{-1}, the Co_3O_4@$MnMoO_4$//AC system has a high energy density of 12.03 Wh kg^{-1}. This demonstrates that Co_3O_4@$MnMoO_4$ is a material with great promise for electrochemical capacitors. The comparison with similar electrode materials for supercapacitors reported

in the literature is shown in Table 1.

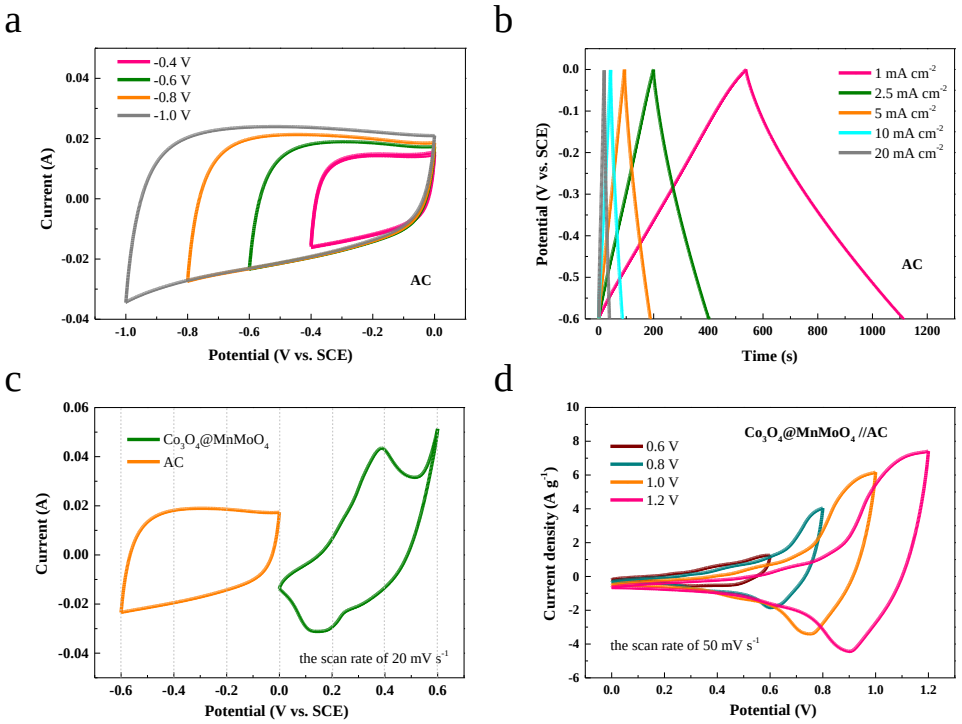

Figure 9. the CV (a, c) and charge-discharge (b) curves of AC electrode in three-electrode system, the CV curves (d) of Co_3O_4@$MnMoO_4$//AC asymmetric electrodes in two-electrode system

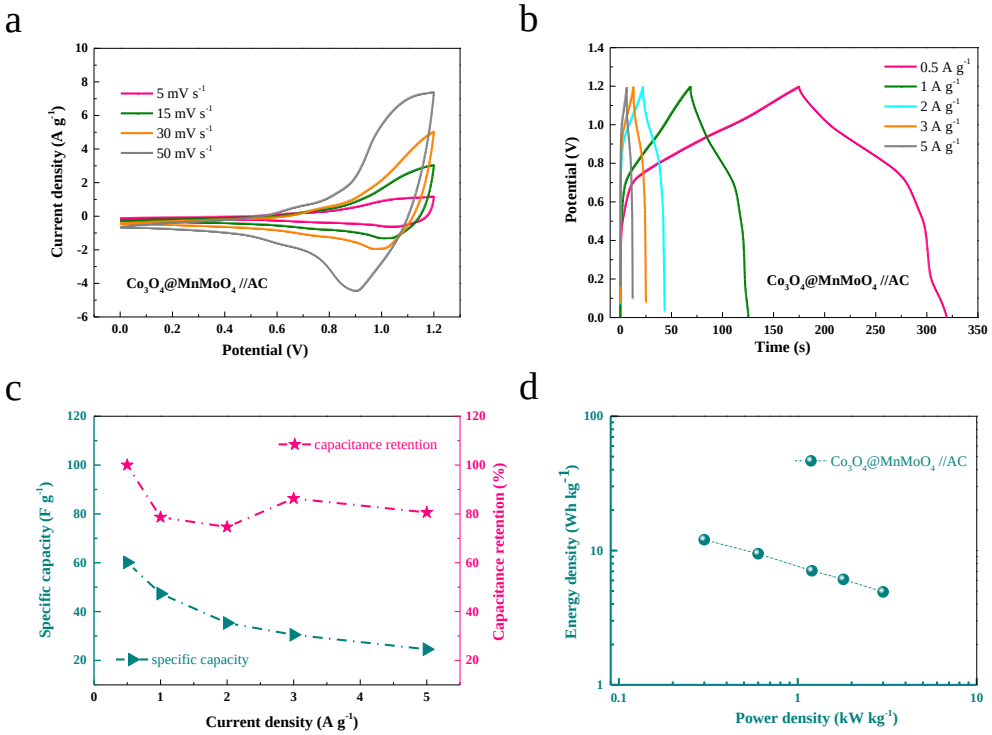

Figure 10. the CV curves (a), galvanostatic charge-discharge curves (b), specific capacities and capacitance retentions (c), and Regone plot (d) of the Co_3O_4@$MnMoO_4$//AC asymmetric electrodes at different scan rates and current densities

Table 1. Performance summarization of supercapacitors reported in the literature.

Materials	Capacitance	Ref.
Co_3O_4@$MnMoO_4$	663.75 Fg^{-1} at current density of 2.5 mA cm^{-2} and the capacitance retained 95.32% after 3000 cycles.	This work
3D-KSPC/Fe_3O_4-DCN	285.4 F g^{-1} at current density of 1 A g^{-1} and the capacitance was kept at 220.5 F g^{-1} after 5000 cycles at 2 A g^{-1}.	[1]
Ni_3S_2/rGO	1886 F g^{-1} at current density of 1.0 A g^{-1}.	[4]
Co_3O_4 nanorods	281 F g^{-1}.	[9]
$Ni(OH)_2$/UGF	119 F g^{-1} at current density of 1 A g^{-1} and the capacitance retained 63.2% after 10000 cycles.	[10]
Co_3O_4/$Ni(OH)_2$	1144 F g^{-1} at 5 mV s^{-1}	[11]
$Co(OH)_2$ nanowire	993 F g^{-1} at current density of 1 A g^{-1}.	[12]
$Co(OH)_2$ nano-flakes	735F g^{-1} in 2 M aqueous KOH.	[14]
β-$Co(OH)_2$	416 F g^{-1} at current of 1 A g^{-1} and the capacitance retained 93% after 500 cycles.	[15]
GO-MnO_2	197.2 F·g^{-1} at 200 mA· g^{-1} and the capacitance retained about 84.1% after 1000 cycles.	[16]
Graphene/MnO_2	energy density of 51.1 Wh kg^{-1} and the capacitance retained 97% after 1000 cycles.	[17]
MnO_2	437 F g^{-1} and the capacitance retained 96% after 10000 cycles.	[18]
Co_3O_4	384.375 F·g^{-1} at the current density of 3 A·g^{-1} and the capacitance retained 96.54% after 1500 cycles.	[21]
PANI-Co_3O_4	1184F·g^{-1}at 1.25A·g^{-1} and the capacitance retained 84.9% after 1000 cycles.	[22]
MoO_2 nanotubes	530 mA h g^{-1} at current density of 1A g^{-1}.	[27]
MoO_2 nanotubes	530 mA h g^{-1} at current density of 1.0 A g^{-1} after 70 cycles.	[29]
$MnMoO_4$ nanorods	168.32 F g^{-1} at current density of 0.5 mA cm^{-2} and the capacitance retained 96% after 2000 cycles.	[37]
$MnMoO_4$·$4H_2O$	1.15 F cm^{-2} at current density of 4 mA cm^{-2} and the capacitance retained 92% after 3000 cycles.	[38]
$CoMoO_4$	32.4 mA h g^{-1} at current density of 1 A g^{-1} and the capacitance retained 85.98% after 5000 cycles.	[40]
Co_3O_4 nanorods	456 F g^{-1} after 500 cycles.	[44]
Co_3O_4/graphene	478 F g^{-1} in 2 M KOH.	[45]
Co_3O_4 nanowires	Energy density of 10.44 Wh kg^{-1},power denity of 7.5 kW kg^{-1} and the capacitance retained 85% after 1000 cycles.	[46]
$MnMoO_4$/graphene	364 F g^{-1} at current density of 2 A g^{-1}.	[47]
Co_3O_4@$NiMoO_4$	636.8 C g^{-1} at 5 mA cm^{-2} and the capacitance retained 84.1% after 2000 cycles.	[50]
NiO@FeCo	90% capacitance retention after 3000 cycles	[52]

4. CONCLUSIONS

In summary, the Co_3O_4@$MnMoO_4$ composites which were first synthesized by a hydrothermal method exhibited higher electrochemical properties than the pure Co_3O_4 nanorods. At a current density of 2.5 mA cm^{-2}, the specific capacities of the Co_3O_4 and Co_3O_4@ $MnMoO_4$ electrodes were 436 Fg^{-1} and 663.75 Fg^{-1}, respectively. After 3000 cycles, the Co_3O_4 and Co_3O_4@$MnMoO_4$ electrodes retained 100% and 95.32% of the initial specific capacity at a current density of 3 A g^{-1}. The two- electrode system of the Co_3O_4@$MnMoO_4$//AC electrodes delivers a high energy density of 12.03 Wh kg^{-1}. Based on the test results, the hybrid Co_3O_4@$MnMoO_4$ composites have good application potential as super capacitors.

COMPETING INTERESTS
The authors declare that there is no conflict of interests regarding the publication of this paper.

DATA AVAILABILITY STATEMENT
The data used to support the findings of this study are included within the article.

ACKNOWLEDGMENTS
This work was financially supported by the National Science Foundation for Distinguished Young Scholars of China (Grant No.61525107), Shanxi Science Foundation of China (Grant No. 201801D221197), School Foundation for North University of China (Grant No. 110246) and Shanxi '1311 project' Key Subject Construction (1331KSC).

References

1. L. Wang, J. Yu, X. Dong, X. Li, Y. Xie, S. Chen, P. Li, H. Hou and Y. Song, *ACS Sustainable Chem. Eng.*, 4 (2016) 1531.
2. M. Ghidiu, M. R. Lukatskaya, M. Zhao, Y. Gogotsi and M. W. Barsoum, *Nature*, 516 (2014) 78.
3. R. Raccichini, A.Varzi, S. Passerini and B. Scrosati, *Nat. Mater.*, 14 (2015) 271.
4. C. Zhang, Y. Huang, S. Tang, M. Deng and Y. Du, *ACS Energy Lett.,* 2 (2017) 759.
5. M. Boota, B. Anasori, C. Voigt, M. Q. Zhao, M. W. Barsoum and Y. Gogotsi, *Adv. Mater.*, 28 (2016) 1517.
6. C. Cui, J. Xu, L. Wang, D. Guo, M. Mao, J. Ma and T.Wang, *ACS Appl. Mater. Interfaces*, 8, 13 (2016) 8568.
7. C. Yuan, X. Zhang, L. Su, B. Gao and L. Shen, *J. Mater. Chem.,* 32 (2009) 5772.
8. J. W. Lang, L. B. Kong, W. J. Wu, Y. C. Luo and L. Kang, *Chem. Commun.,* 35 (2008) 4213.
9. G. Wang, X. Shen, J. Horvat, B. Wang, H. Liu, D. Wexler and J. Yao, *J. Phys. Chem. C*, 113, 11 (2009) 4357.
10. J. Ji, L.L.Zhang, H. Ji, Y. Li, X. Zhao, X. Bai, X. Fan, F. Zhang and R. S. Ruoff, *ACS Nano*, 7, 7 (2013) 6237.
11. J. H. Zhong, A. L. Wang, G. R. Li, J. W. Wang, Y. N. Ou and Y. X. Tong, *J. Mater. Chem.*,12 (2012) 5656.
12. T. Xue, X. Wang and J. M. Lee, *J. Power Sources*, 201 (2012) 382.
13. F. Cao, G. X. Pan, P. S. Tang and H. F. Chen, *J. Power Sources*, 216 (2012) 395.
14. L. B. Kong, J. W. Lang, M. Liu, Y. C. Luo and L. Kang, *J. Power Sources*, 194, 2 (2009)1194.
15. C. Mondal, M. Ganguly, P. K. Manna, S. M. Yusuf and T. Pal, *Langmuir*, 29, 29 (2013) 9179.
16. S. Chen, J. Zhu, X. Wu, Q. Han and X. Wang, *ACS Nano*, 4, 5 (2010) 2822.
17. Z. Fan, J.Yan, T. Wei, L. Zhi, G. Ning, T. Li and F. Wei, *Adv. Funct. Mater.*, 21, 12 (2011) 2366.
18. X. Tao, J. Du, Y. Sun, S. Zhou, Y. Xia, H. Huang, Y. Gan, W. Zhang and X. Li, *Adv. Funct. Mater.*,

23, 37 (2013) 4745.
19. W. Wei, X. Cui, W. Chen and D. G. Ivey, *Chem. Soc. Rev.*, 3 (2011) 1697.
20. M. Lindo, A. J. Vizcaíno, J. A. Calles, and A. Carrero, *Int. J. Hydrogen Energy*, 35, 11 (2010) 5895.
21. Y. Li, Z. Hai, X. Hou, H. Xu, Z. Zhang, D. Cui, C.Xue and B. Zhang, *J. Nanomater.*, 2017.
22. Z. Hai, L. Gao, Q. Zhang, H. Xu, D. Cui, Z. Zhang, D. Tsoukalas, J. Tang, S. Yan and C. Xue, *Appl. Surf. Sci.*, 361 (2015) 57.
23. A. S. Arico, P. Bruce, B. Scrosati, J. M. Tarascon and W. V. Schalkwijk, *Nat. Mater.*, 4 (2005).
24. P. Poizot, S. Laruelle, S. Grugeon, L. Dupont and J. M. Tarascon, *Nature*, 407 (2000) 496.
25. P. J. Hall, M. Mirzaeian, S. I. Fletcher, F. B. Sillars, A. J. R. Rennie, G. O. Shitta-Bey, G. Wilson, A. Cruden and R. Carter, *Energy Environ. Sci.*, 9 (2010) 1238.
26. G. Wang, L. Zhang, L and J. Zhang, *Chem. Soc. Rev.*, 2 (2012) 797.
27. L. L. Zhang and X. S. Zhao, *Chem. Soc. Rev.*, 9 (2009) 2520.
28. J. H. Ku, J. H. Ryu, S. H. Kim, O. H. Han and S. M. Oh, *Adv. Funct. Mater,* 22, 17 (2012) 3658.
29. H. J. Zhang, J. Shu, K. X. Wang, X. T. Chen, Y. M. Jiang, X. Wei and J. S. Chen, *J. Mater. Chem. A*, 2 (2014) 80.
30. J. Park, O. Choi, M. J. Lee, M. H. Kim, T. Lim, K. H. Park, J. Jang, S. M. Oh, S. K. Cho and J. J. Kim, *Electrochim. Acta*, 132 (2014) 338.
31. D. Koziej, M. D. Rossell, B. Ludi, A. Hintennach, P. Novak, J. D. Grunwaldt, M. Niederberger, *Small*, 7, 3 (2011) 377.
32. P. Meduri, E. Clark, J. H. Kim, E. Dayalan, G. U. Sumanasekera and M. K. Sunkara, *Nano Lett.*, 12, 4 (2012) 1784.
33. L. Guo and Y. Wang, *J. Mater. Chem. A*, 8 (2015) 4706.
34. S.Balendhran, S. Walia, H. Nili, J. Z. Ou, S. Zhuiykov, R. B. Kaner, S. Sriram, M. Bhaskaran and K. Kalantar-zadeh, *Adv. Funct. Mater*, 23, 32 (2013) 3952.
35. K. Chang and W. Chen, *ACS Nano*, 5 (2011) 4720-4728.
36. Y. Ding, Y. Wan, Y. L. Min, W. Zhang, and S. H. Yu, *Inorg. Chem.*, 47(2008), 7813-7823.
37. G. K. Veerasubramani, K. Krishnamoorthy, R. Sivaprakasam, and S. J. Kim, *Mater. Chem. Phys.*, 147 (2014) 836-842.
38. Y. Cao, W. Li, K. Xu, Y. Zhang, T. Ji, R. Zou, J. Yang, Z. Qin, and J. Hu, *J. Mater. Chem. A.*, 48 (2014) 20723-20728.
39. W. Xiao, J. S. Chen, C. M. Li, R. Xu, and X. W. Lou, *Chem. Mater.*, 22 (2010) 746-754.
40. M. Li, S. Xu, C. Cherry, Y. Zhu, D. Wu, C. Zhang, X. Zhang, R. Huang, R. Qi, L. Wang, P. Chu, *J. Mater. Chem. A.*, 26 (2015) 13776-13785.
41. Y. Sun, X. Hu, W. Luo, and Y. Huang, *J. Mater. Chem.*, 43 (2011) 17229.
42. K. Ben-Kamel, N. Amdouni, H. Groult, A. Mauger, K. Zaghib, and C. M. Julien, *J. Power Sources*, 202 (2012) 314-321.
43. X. Hu, W. Zhang, X. Liu, Y. Mei, and Y. Huang, *Chem. Soc. Rev.*, 8 (2015) 2376-2404.
44. L. Cui, J. Li, and X. G. Zhang, *J. Appl. Electrochem,* 39 (2009) 1871.
45. B. Wang, Y. Wang, J. Park, H. Ahn, and G. Wang, *J. Alloys Compd.*, 509 (2011) 7778.
46. W. Liu, X. Li, M. Zhu, and X. He, *J. Power Sources*, 28 (2015) 179.
47. D. Ghosh, S. Giri, M. Moniruzzaman, T. Basu, M. Mandal, and C. K. Das, *Dalton Trans.,* 28 (2014) 11067.
48. K. K. Purushothaman, M. Cuba, and G. Muralidharan, *Mater. Res. Bull.*, 47 (2012) 3348.
49. B. Guan, W. Sun, and Y. Wang, *Electrochim. Acta,* 190 (2016) 354.
50. Y. Zhang, Y. Yang, L. Mao, D. Cheng, Z. Zhan, and J. Xiong, *Mater. Lett.,* 182 (2016) 298.
51. Y. Li, X. Hou, Z. Zhang, Z. Hai, H. Xu, D. Cui, S. Zhuiykov and C. Xue, *Appl. Surf. Sci.*, 436 (2018) 242.
52. L. Gao, K.Cao, H. Zhang, P. Li, J. Song, J. U. Surjadi, Y. Li, D. Sun and Y. Lu, *J. Mater. Chem. A*, 32 (2017).
53. Y. Chen, Y. Li, Z. Hai, Y. Li, S. Kan, J. Chen, X. Chen, S. Zhuiykov, D. Cui and C. Xue, *Appl. Surf.*

Sci., 452 (2018) 413.
54. L. Gao, H. Zhang, J. U. Surjadi, P. Li, Y. Han, D. Sun and Y. Lu, *Nanoscale*, *5 (*2018) 2613.